FULL POTENTIAL UNSTEADY COMPUTATIONS INCLUDING AEROELASTIC EFFECTS

Vijaya Shankar
Rockwell International Science Center
Thousand Oaks, California

Hiroshi Ide
Rockwell Aircraft Operations
Los Angeles, California

SUMMARY

A unified formulation is presented based on the full potential framework coupled with an appropriate structural model to compute steady/unsteady flows over rigid/flexible configurations for across the Mach number range (subsonic to supersonic). The unsteady form of the full potential equation in conservation form is solved using an implicit scheme maintaining time accuracy through internal Newton iterations. A flux biasing procedure based on the unsteady sonic reference conditions is implemented to compute hyperbolic regions with moving sonic and shock surfaces. The wake behind a trailing edge is modeled using a mathematical cut across which the pressure is satisfied to be continuous by solving an appropriate vorticity convection equation. An aeroelastic model based on the generalized modal deflection approach interacts with the nonlinear aerodynamics and includes both static as well as dynamic structural analyses capability. Figure 1 shows a schematic of the coupling process. Some of the topics to be discussed are 1) mechanism for coupling the aerodynamic and the aeroelastic equations, 2) update of geometry and grid at each time level to maintain time accuracy, and 3) prediction of flutter point dynamic pressure.

Results are presented for rigid and flexible configurations at different Mach numbers ranging from subsonic to supersonic conditions. The dynamic response of a flexible wing below and above its flutter point is demonstrated.

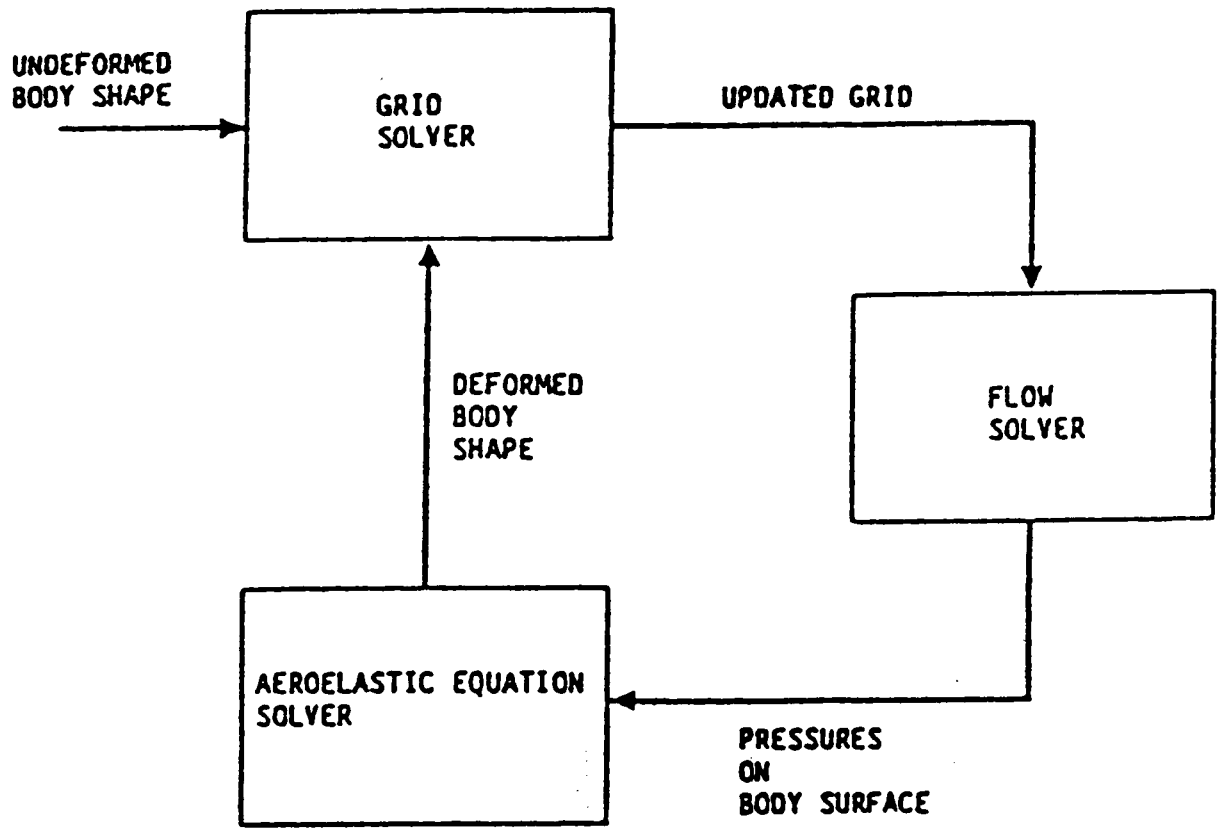

Fig. 1. Schematic of CFD/Aeroelastic Coupling

AERODYNAMIC FORMULATION

The conservation law form of the time–dependent full potential equation cast in an arbitrary coordinate system (τ, ζ, η, ξ) is written as

$$\bar{\rho}_\tau + \bar{E}_\zeta + \bar{F}_\eta + \bar{G}_\xi = 0$$

where

$$\begin{aligned} \bar{\rho} &= \frac{\rho}{J} \\ \bar{E} &= (\rho\zeta_t + E\zeta_x + F\zeta_y + G\zeta_z)/J \\ \bar{F} &= (\rho\eta_t + E\eta_x + F\eta_y + G\eta_z)/J \\ \bar{G} &= (\rho\xi_t + E\xi_x + F\xi_y + G\xi_z)/J \end{aligned} \tag{1}$$

and J, Jacobian for the transformation, is given by

$$J = \partial(\tau, \zeta, \eta, \xi)/\partial(t, x, y, z)\,.$$

The density ρ is given by Bernoulli's law

$$\begin{aligned} \rho^{\gamma-1} = 1 - \frac{\gamma-1}{2} M_\infty^2 [&2\phi_\tau + (U + \zeta_t) \\ &+ (V + \eta_t)\phi_\eta + (W + \xi_t)\phi_\xi - 1] \end{aligned} \tag{2}$$

where U, V, and W are the contravariant velocities.

Associating the subscripts i,j,k with the ζ,η,ξ directions, a numerical approximation to Eq. (1) can be written in the semidiscrete conservation law form given by

$$\begin{aligned} &\left(\frac{\rho}{J}\right)_\tau + \left(\tilde{E}_{i,j,k+1/2} - \tilde{E}_{i,j,k-1/2}\right) \\ &\quad + \left(\tilde{F}_{i,j+1/2,k} - \tilde{F}_{i,j-1/2,k}\right) \\ &\quad + \left(\tilde{G}_{i+1/2,j,k} - \tilde{G}_{i-1/2,j,k}\right) = 0 \end{aligned} \tag{3}$$

where $\tilde{E},\tilde{F},\tilde{G}$ are representative fluxes approximating the real fluxes $\bar{E},\bar{F},\bar{G}$ of Eq. (1).

NEWTON ITERATION

In terms of the velocity potential, Eq. (3) can be represented as

$$R(\phi) = 0 \tag{4}$$

where ϕ is the unknown to be solved at every grid point (i, j, k) in the current $(n+1)$ time plane. The Newton iteration for solution to Eq. (4) is

$$R(\phi_*) + \left(\frac{\partial R}{\partial \phi}\right)_{\phi=\phi_*} \cdot \Delta\phi = 0 \tag{5}$$

where ϕ_* is the currently available ϕ at the $(n+1)$ level and $\Delta\phi = \phi - \phi_*$. At convergence, $\Delta\phi$ will approach zero driving ϕ to ϕ^{n+1}. (See Fig. 2).

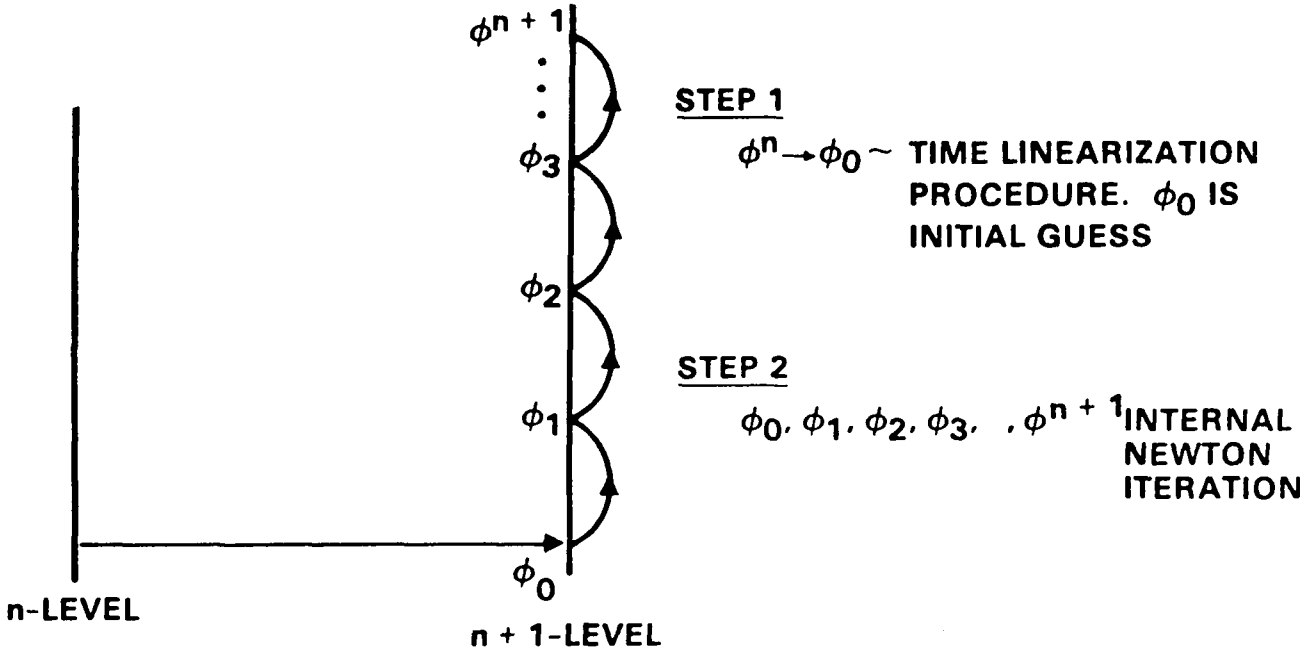

Fig. 2. Update of ϕ Based on Newton Iteration

TIME LINEARIZATION

Treatment of $\frac{\partial}{\partial\tau}\left(\frac{\rho}{J}\right)$ in Eq. (1)

$$\frac{\partial}{\partial\tau}\left(\frac{\rho}{J}\right) = \frac{(a_1 - b_1)\left\{\left(\frac{\rho}{J}\right)^{n+1} - \left(\frac{\rho}{J}\right)^{n}\right\} - b_1\left\{\left(\frac{\rho}{J}\right)^{n} - \left(\frac{\rho}{J}\right)^{n-1}\right\}}{a_1\Delta\tau_1 - b_1(\Delta\tau_1 + \Delta\tau_2)} \tag{6}$$

where

$$a_1 = (\Delta\tau_1 + \Delta\tau_2)^2\,;\ \Delta\tau_1 = \tau^{n+1} - \tau^{n}\,;\ \Delta\tau_2 = \tau^{n} - \tau^{n-1}\,.$$

The unknown quantity in Eq. (6) is ρ^{n+1}. Following Eq. (5), this is written as

$$\rho = \rho(\phi_*) + \left(\frac{\partial\rho}{\partial\phi}\right)_{\phi=\phi_*}\Delta\phi \tag{7}$$

where $\Delta\phi = \phi - \phi_*$, and

$$\left(\frac{\partial\rho}{\partial\phi}\right)_{\phi=\phi_*} = \left[-\frac{\rho}{a^2}\left\{\frac{1}{\Delta\tau_1} + U\frac{\partial}{\partial\zeta} + V\frac{\partial}{\partial\eta} + W\frac{\partial}{\partial\xi}\right\}\right]_{\phi=\phi_*} \tag{8}$$

is a differential operator. The speed of sound is denoted by a.

FLUX BIASING

Equation (3) requires evaluation of $\tilde{E}$, $\tilde{F}$, and $\tilde{G}$ at various spatial half node points. As mentioned earlier, $\tilde{E}$ represents $\bar{E}$ appearing in Eq. (1). The fluxes are defined in the following manner.

$$\tilde{E} = \tilde{\rho}\frac{U}{J} \quad ; \quad \tilde{F} = \tilde{\rho}\frac{V}{J} \quad ; \quad \tilde{G} = \tilde{\rho}\frac{W}{J} \tag{9}$$

where $\tilde{\rho}$ is an upwind biased value of density, designed to produce the necessary artificial viscosity for treatment of hyperbolic regions.

$$\tilde{\rho} = \frac{1}{q}\left[(\rho q) \pm \left\{\frac{U}{Q}\frac{\partial}{\partial\zeta} + \frac{V}{Q}\frac{\partial}{\partial\eta} + \frac{W}{Q}\frac{\partial}{\partial\xi}\right\}(\rho q)^{-}\right] \tag{10}$$

where $Q = \sqrt{U^2 + V^2 + W^2}$.

The quantity $(\rho q)^{-}$ appearing in Eq. (10) is defined to be

$$\begin{aligned} (\rho q)^{-} &= \rho q - \rho^* q^* \qquad \text{if } q > q^* \\ &= 0 \qquad\qquad\quad \text{if } q \le q^* . \end{aligned} \tag{11}$$

The quantities $\rho^8 q^*$, ρ^*, and q^* represent sonic values of the flux, density, and total velocity, respectively. These quantities are evaluated at half node grid points. (See Fig. 3).

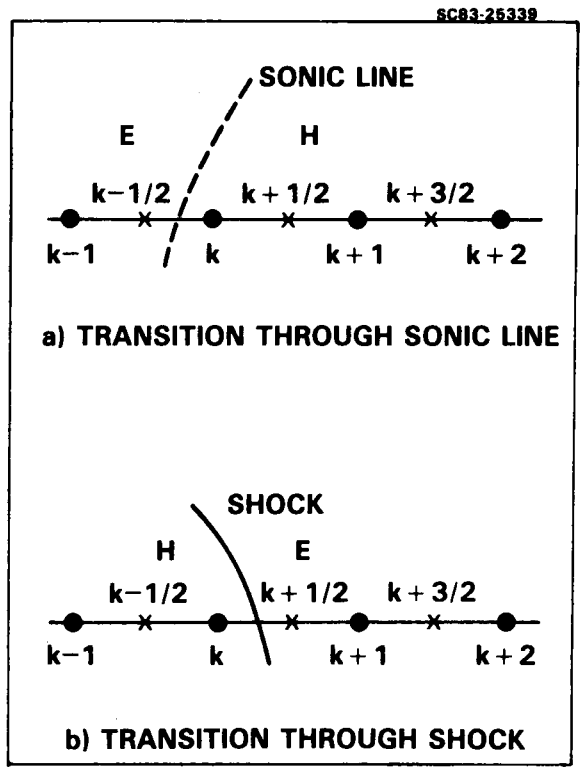

Fig. 3. Notation for Flux Biasing

AEROELASTIC MODEL

The aeroelastic model is based on the generalized modal approach. In the physical space, the structural equation is written as

$$[m]\ddot{z} + [c]\dot{z} + [k] = \{f\}$$

where m, c, k, and f represent the mass, damping, stiffness, and force, respectively. The structural deflection is given by z. Using the generalized mode shape, ϕ, one can rewrite the above equation as

$$M\{\ddot{q}\} + [C]\{\dot{q}\} + [K]\{q\} = \{F\}$$

where M, C, and K are generalized mass, damping, and stiffness matrices and $\{F\}$ is the generalized aerodynamic force. These are defined by

$$M = \phi^T m \phi \quad ; \quad K = \phi^T k \phi \quad ,$$
$$C = \phi^T c \phi \quad , \quad F = \phi^T f \quad \text{and} \quad z = \phi q \quad ,$$

where q is the generalized deflection.

STATIC FLEXIBLE CASE

The flexibility of the structure comes into the calculation through stiffness (K) and generalized mode shapes (ϕ). The steps involved in computing the static flexible equilibrium aerodynamics are given below:

1. Solve rigid aerodynamics for lift force.
2. Solve $Kq = F \Rightarrow \{z\} = [\phi]\{q\}$.
3. Increment $\{z\}$ in smaller steps and compute modified aerodynamic force, Figure 4.
4. Repeat Step 2.
5. Continue until $\{z\}$ and lift converge.

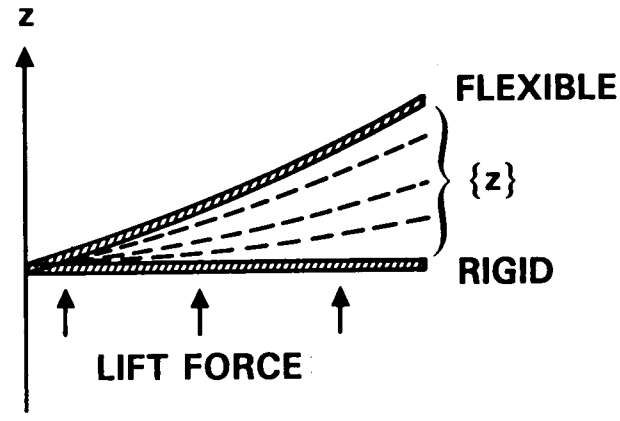

Fig. 4. Incremental Shape Change for Static Flexible Calculation

DYNAMIC FLEXIBLE CASE

The aerodynamics and the structural response are computed in a time accurate fashion using internal Newton iterations. The various steps involved in this computation are

1. Compute rigid aerodynamics.
2. Compute static flexible for a given dynamic pressure Q.
3. Set up an initial perturbance by perturbing either q or $\dot{q}$ of any mode.
4. Solve $M\ddot{q} + C\dot{q} + Kq = F \Rightarrow \{z\}$.
5. Compute x_τ, y_τ, z_τ on the surface.
6. Define x_τ, y_τ, z_τ for each field grid point allowing their values to go to zero at outer boundary, Figure 5.
7. Compute new grid location $x^{n+1} = x^n + x_\tau \Delta\tau, \cdots$ and new metrics.
8. Converge aerodynamics using internal Newton iteration.
9. Repeat Step 4. (For prediction of flutter Q gradually vary Q and monitor generalized modal deflections.)

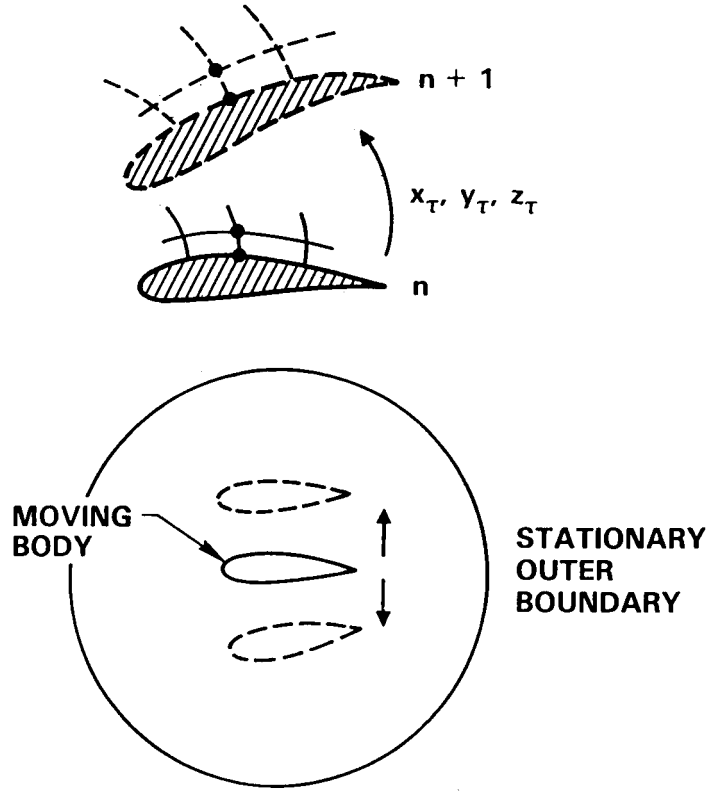

Fig. 5. Grid Update for Dynamic Flexible Calculations

OTHER FEATURES OF AERODYNAMIC/AEROELASTIC PROCEDURE

- Aerodynamics solved by triple approximate factorization scheme $\frac{\partial R}{\partial \phi} = L_\zeta L_\xi L_\eta$
- Wake cut modeled by unsteady vorticity convection equation
- Implicit boundary conditions
- Internal Newton iteration for time accuracy.

Code Capabilities

- Static Rigid
- Dynamic Rigid
- Static Flexible
- Dynamic Flexible

FLEXIBLE WING MODEL

Figure 6 shows the planform shape of a flexible low aspect ratio fighter wing. A sectional airfoil profile is also shown in Fig. 6. Note that there are two bumps in the lower section which are due to the leading edge and trailing edge control surface actuators. This model was designed and built by Rockwell and currently is being tested in NASA Langley Research Center's 16 foot TDT wind tunnel.

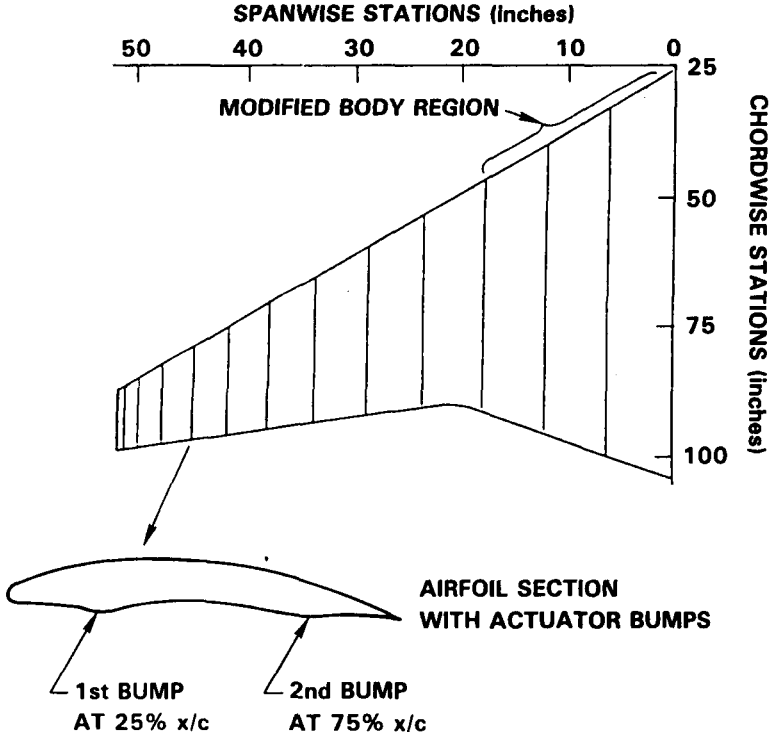

Fig. 6. Planform Shape of a Flexible Fighter Wing

NATURAL MODE SHAPES

Figure 7 shows the first ten natural frequency mode shapes for aeroelastic analysis. Mode shapes are prescribed at every grid point on the wing surface.

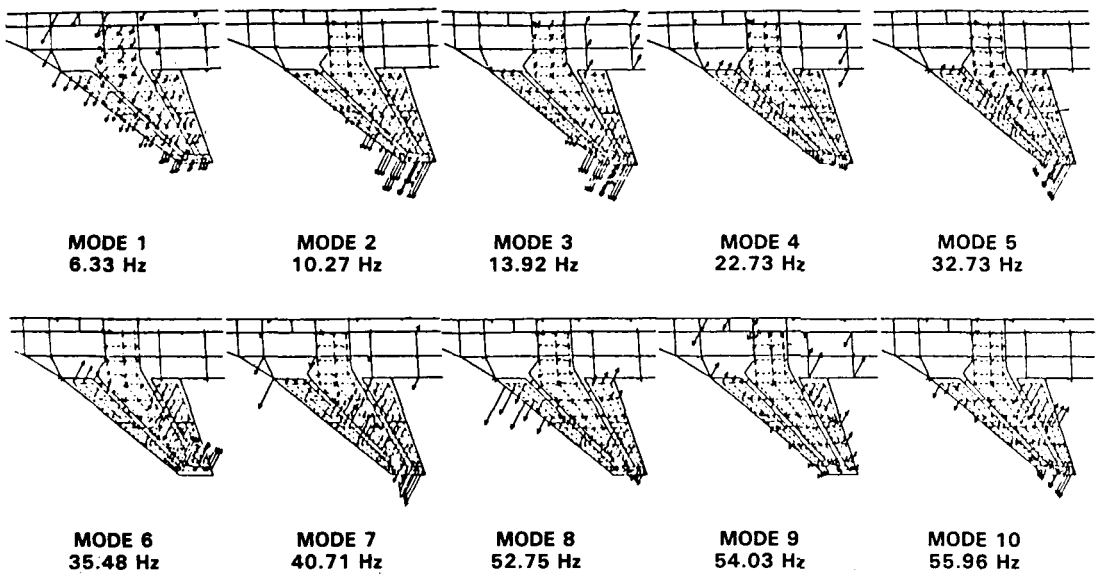

Fig. 7. Selected Mode Shapes for Aeroelastic Analyses

RESULTS FOR STATIC FLEXIBLE CASE

Figure 8 shows results for a static flexible computation at $M_\infty = 1.15$, $\alpha = 6°$ for two different dynamic pressure conditions. $Q = 0$ corresponds to the rigid case. The deflected shape of the wing for $Q = 288$ psf shows the nose down rotation of the airfoil near the wing tip resulting in tip load reduction. This is essential for the wing to be aeroelastically stable.

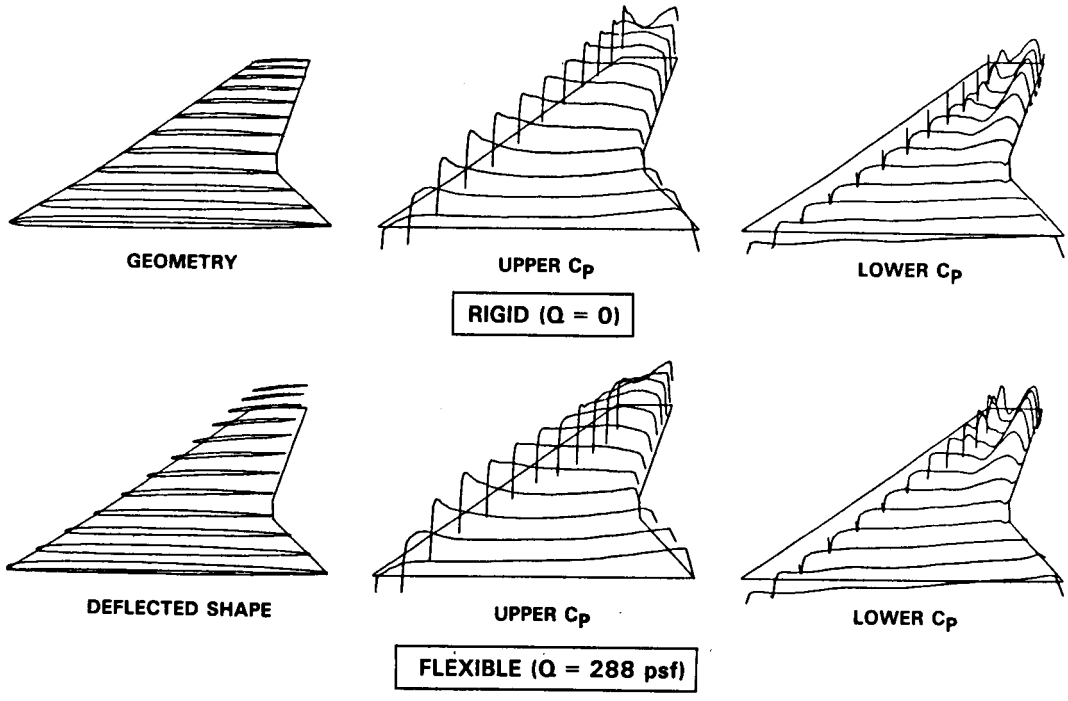

Fig. 8. Static Flexible Computation, $M_\infty = 1.15$, $\alpha = 6°$

C_L VERSUS α FOR STATIC FLEXIBLE

The C_L versus α curves at two different Mach numbers are shown in Fig. 9. Table 1 shows the change in total lift coefficient between rigid and flexible cases for different Mach numbers, angles of attack, and Q conditions.

M	α	Q(psf)	$C_{L_{test}}$	$C_{L_{flex}}$	$C_{L_{rigid}}$
1.05	1.6	335	0.0785	0.0800	0.1450
1.15	0.5	230	0.0433	0.0400	0.0685
0.90	0.0	220	0.0446	0.0441	0.0637

Table 1. Comparison of Lift Coefficients between Rigid and Flexible Calculations

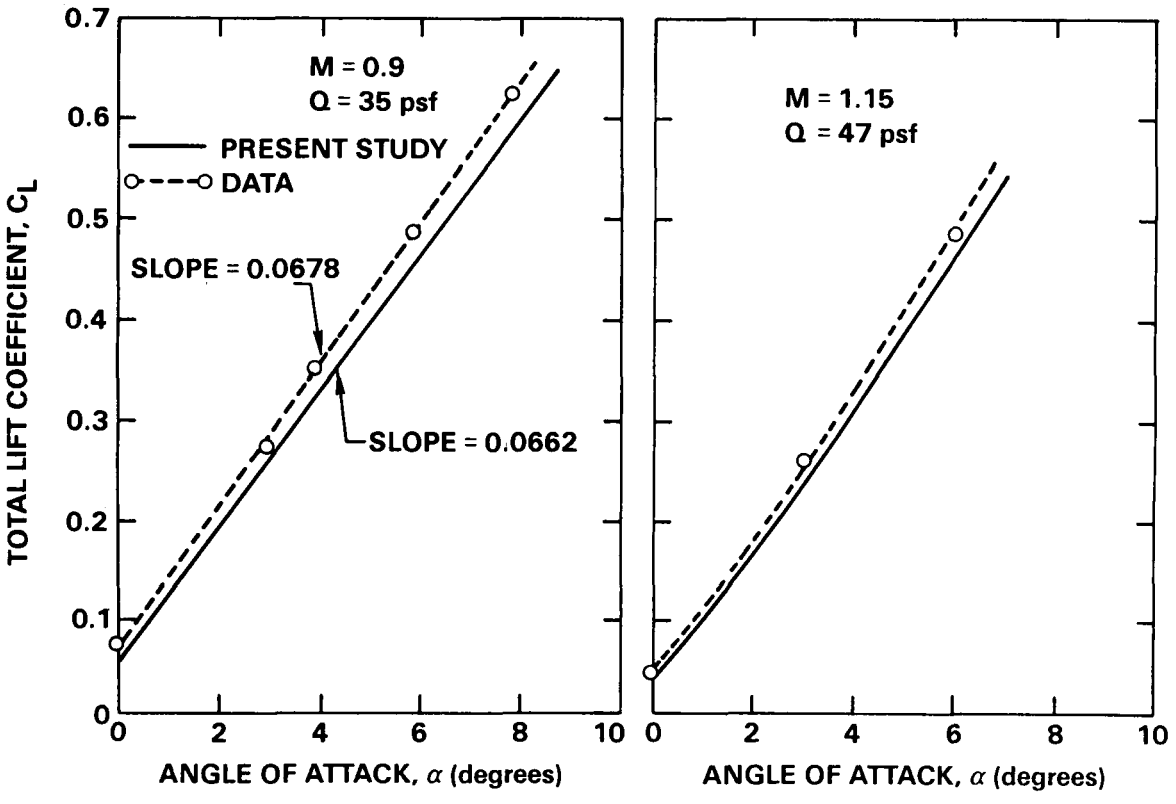

Fig. 9. C_L versus α for the Flexible Wing

STATIC FLEXIBLE WITH DEFLECTED CONTROLS

Figure 10 shows a similar static aeroelastic calculation with leading and trailing edge control surfaces deflected. Also shown are the surface chordwise pressure distributions at various span stations and a cross section of the wing with deflected control surfaces. The span stations where the deflected control surfaces are present are drastically altered.

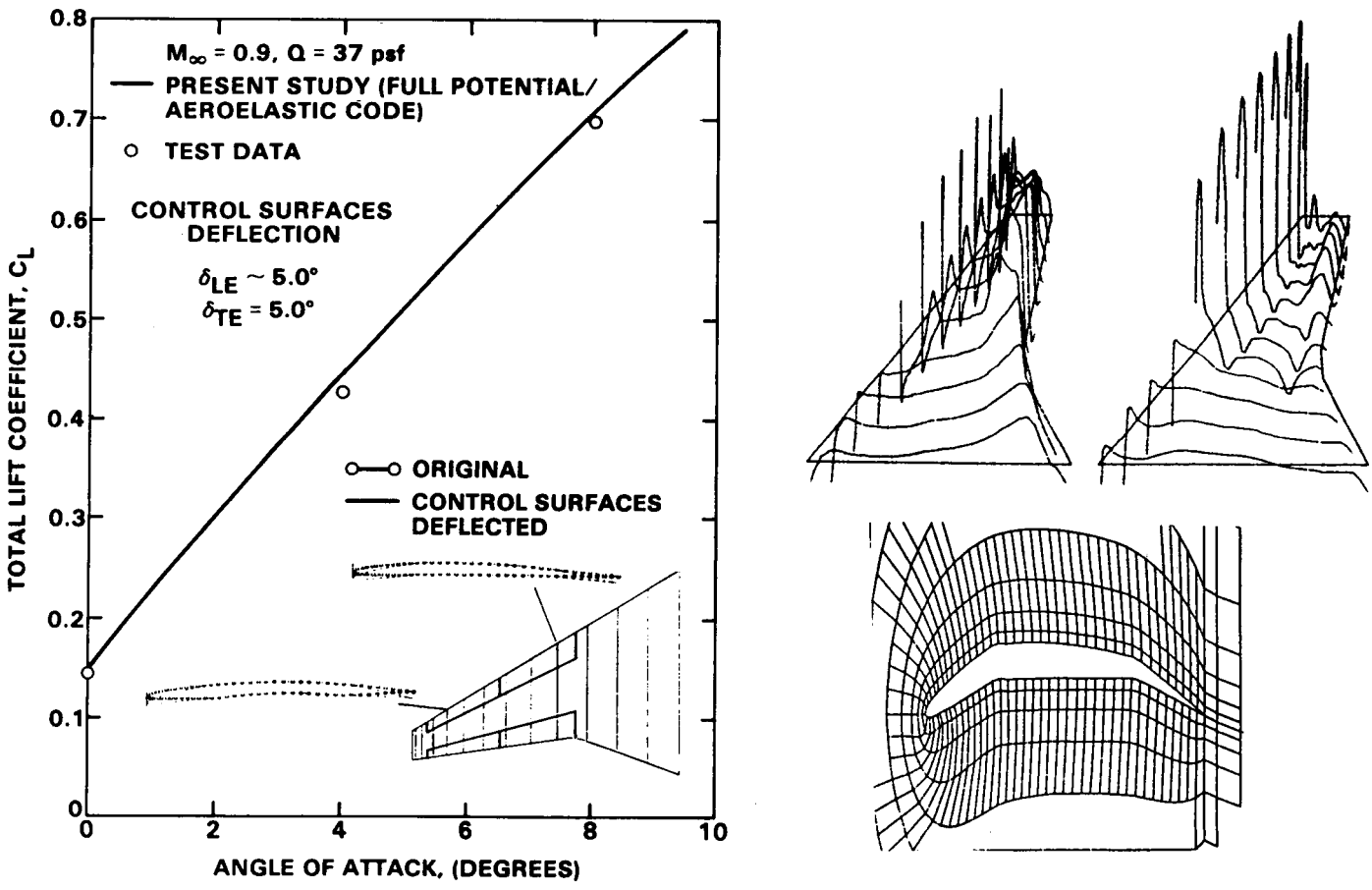

Fig. 10. Static Aeroelastic Computations with Deflected Control Surfaces

DYNAMIC FLEXIBLE CASE

Figures 11–13 show results for dynamic aeroelastic computations at three different dynamic pressures (Q). Figure 11 is for $Q < Q_{\text{Flutter}}$. The structure is aerodynamically stable as shown by the decaying amplitudes of various quantities. Figure 12 is exactly at the flutter dynamic pressure. The value for the flutter Q was obtained by the nonlinear aerodynamics/aeroelastic code through numerical search. Exactly at the flutter Q, the dynamic response of the structure does not decay as shown by results of Fig. 12. Figure 13 illustrates the structural response above the flutter Q. The structure is aerodynamically unstable as shown by the growing amplitudes of various quantities.

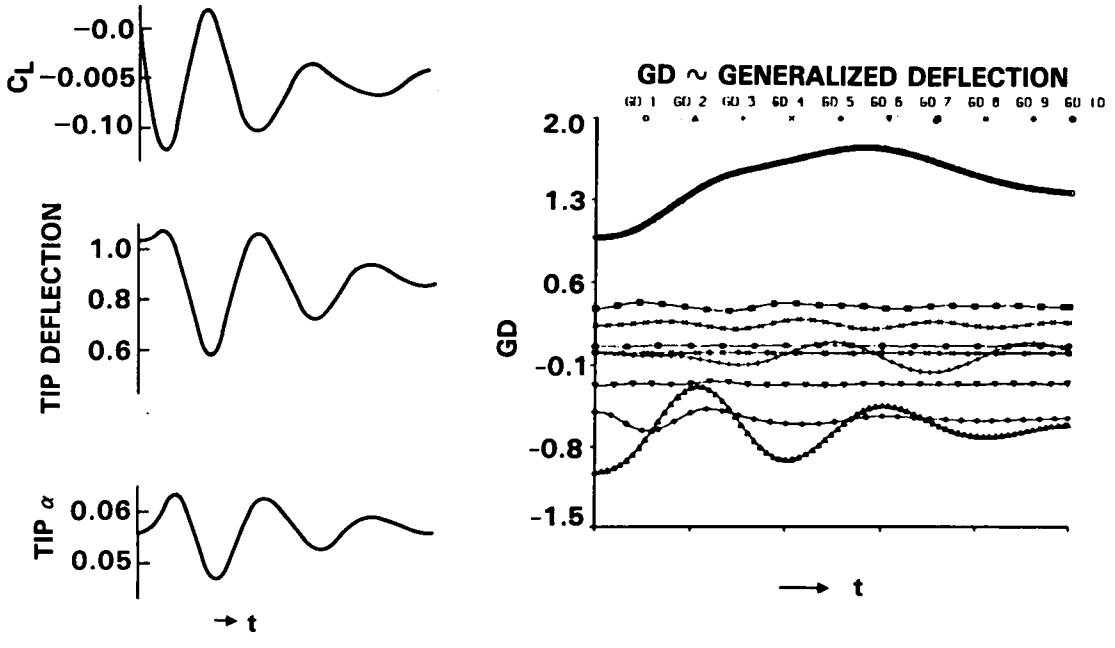

Fig. 11. Dynamic Flexible Computation – below Flutter, $M_\infty = 1.15$, $\alpha = 0°$, $Q = 360$ psf

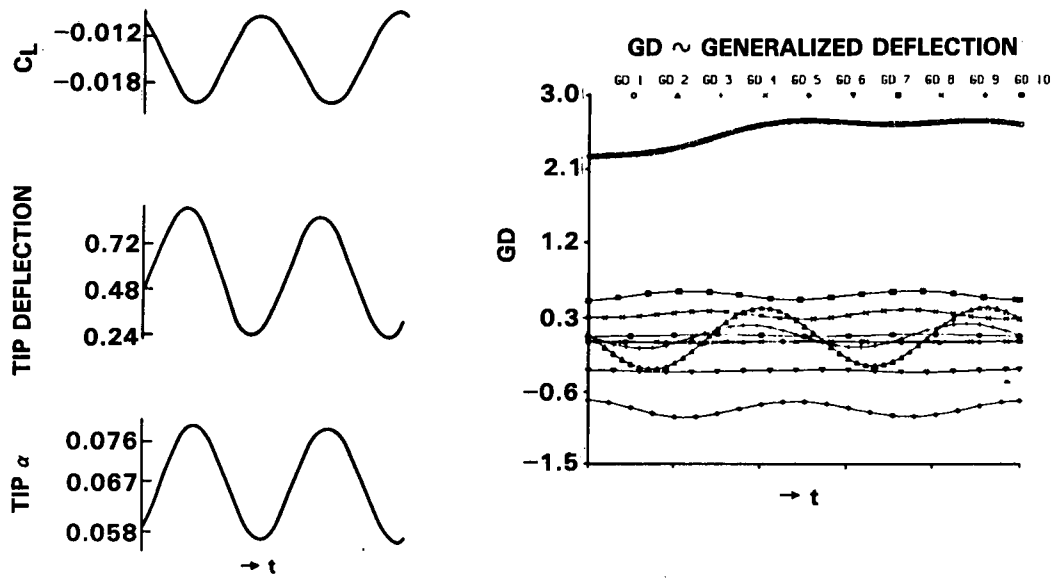

Fig. 12. Dynamic Flexible Computation – at Flutter Point, $M_\infty = 1.15$, $\alpha = 0°$, $Q = 490$ psf

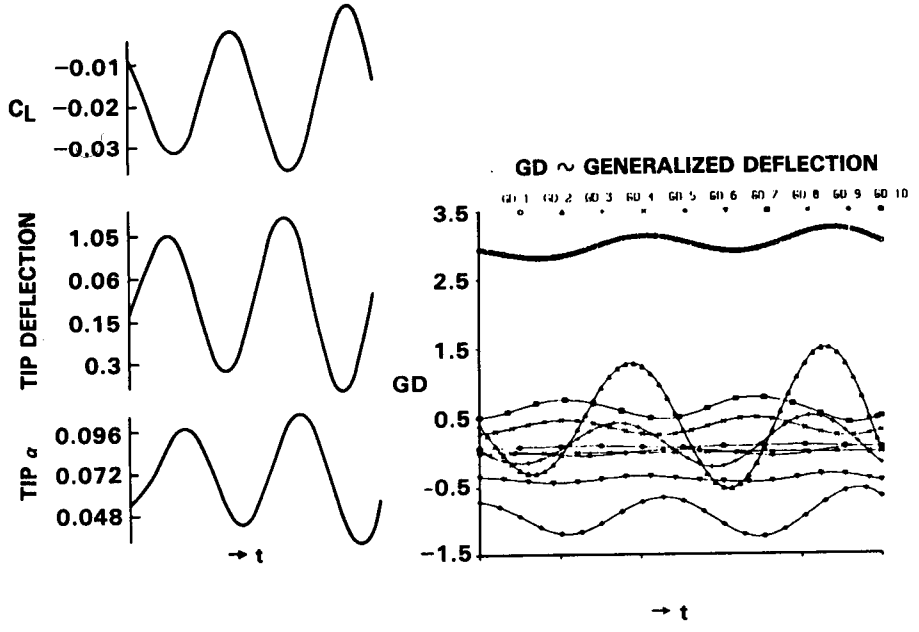

Fig. 13. Dynamic Flexible Computation – above Flutter, $M_\infty = 1.15$, $\alpha = 0°$, $Q = 550$ psf